



HAL
open science

H₂ Dissociation and Oxygen Vacancy Formation on Ce₂O₃ Surfaces

O. Matz, M. Calatayud

► **To cite this version:**

O. Matz, M. Calatayud. H₂ Dissociation and Oxygen Vacancy Formation on Ce₂O₃ Surfaces. Topics in Catalysis, 2019, 62 (12-16), pp.956-967. 10.1007/s11244-019-01183-0 . hal-02496932

HAL Id: hal-02496932

<https://hal.science/hal-02496932>

Submitted on 3 Mar 2020

HAL is a multi-disciplinary open access archive for the deposit and dissemination of scientific research documents, whether they are published or not. The documents may come from teaching and research institutions in France or abroad, or from public or private research centers.

L'archive ouverte pluridisciplinaire **HAL**, est destinée au dépôt et à la diffusion de documents scientifiques de niveau recherche, publiés ou non, émanant des établissements d'enseignement et de recherche français ou étrangers, des laboratoires publics ou privés.

H₂ dissociation and oxygen vacancy formation on Ce₂O₃ surfaces

O. Matz[†]; M. Calatayud^{†*}

[†]Sorbonne Université, CNRS, Laboratoire de Chimie Théorique, LCT, F. 75005 Paris, France

*Corresponding author:

Dr. Hab. M. Calatayud

Laboratoire de Chimie Théorique

Sorbonne Université

4, Place Jussieu case 137

75252 Paris cedex 5 – France

Phone: +33 1 44 27 25 05

Fax: +33 1 44 27 41 17

e-mail: calatayu@lct.jussieu.fr

ORCID ID: 0000-0003-0555-8938

Abstract

H₂ dissociation on ceria (CeO₂) has attracted much attention in the last years because of its potential application in catalysis for hydrogenation reactions, as well as for the stabilization of hydride bulk and surface species. The ability of ceria to split hydrogen is strongly dependent on the surface morphology. However, to the best of our knowledge, the reactivity of the cerium sesquioxide Ce₂O₃ A-type (hexagonal structure with space group $P\bar{3}m1$) has not been previously addressed. In the present study, we investigate (i) the formation of oxygen vacancies in A-Ce₂O₃ bulk and (ii) the effect of the surface topology in the H₂ dissociation and in the oxygen vacancy formation for the four most stable

surfaces of A-Ce₂O₃: (0001), (01-11), (11-20) and (11-21). Our results indicate a significant decrease of the energetic barrier for the hydrogen dissociation compared to stoichiometric CeO₂, with an activation energy of ~0.1 eV. Interestingly, Ce₂O₃ surfaces lead to a heterolytic product with hydride species more stable than the homolytic product, which is the opposite behavior found in CeO₂. These results suggest a better performance of Ce₂O₃ than CeO₂ for H₂ dissociation and provide insight in the nature of hydride-Ce₂O₃ interfaces that could be important intermediates in the formation of CeH_x phases from cerium oxide.

Keywords: reduced ceria, Ce₂O₃, hydride, oxygen vacancy, hydrogen, dissociation

1. Introduction

Cerium oxides (CeO_x with $1.5 \leq x \leq 2.0$) are promising materials widely used in the fields of catalysis^{1,2} and energy³ as well as other technological applications⁴ due to its special electronic properties.⁵ The reducibility of ceria, i.e. its ability to release and store oxygen, is closely related to the facile and reversible change of oxidation states of Ce atoms ($\text{Ce}^{4+} \leftrightarrow \text{Ce}^{3+}$) and determines in great manner its properties.⁶⁻⁹ In this sense, partial reduction (CeO_{2-x} , $0 < x < 0.5$) may lead to different behavior than complete reduction (Ce_2O_3). The former is related to the presence of oxygen vacancies without change of the crystalline structure (typically a fluorite) whereas the latter corresponds to the limit case where all the Ce atoms are reduced into Ce^{3+} with a sesquioxide A-type (hexagonal) structure.¹⁰ In the last years, much effort was put in the comprehension of the partial reduction impact on the ceria surface property¹¹⁻¹⁶ and reactivity¹⁷⁻²¹, with much less insight in Ce_2O_3 compositions. In standard conditions of pressure and temperature, Ce_2O_3 is not a stable material but recent development of new experimental techniques and protocols make possible the synthesis of Ce_2O_3 particles.²²⁻²⁵ Furthermore, the reduction of (111)- CeO_2 can also lead to the formation of (0001)-A- Ce_2O_3 .^{26,27} However, to the best of our knowledge, the reactivity of Ce_2O_3 surfaces has not been addressed in the literature. In this work, the four most stable terminations of Ce_2O_3 were investigated, and a detailed description of the geometry, energetics and electronic structure is provided together with an analysis of its reactivity towards H_2 dissociation.

Recently, ceria has been successfully used in hydrogenation processes²⁸⁻³¹ with high activity and selectivity, thus opening new avenues in hydrogenation catalysis application in the absence of noble metals.³¹⁻³⁸ The mechanism of the H_2 dissociation on the (111)- CeO_2 surface was proposed by García-Melchor et al.³³ and Fernández-Torre et al.³⁴: the H_2 molecule dissociates according to a heterolytic pathway forming a hydride/proton pair (Ce-H/OH) which is 0.7-0.8 eV endothermic, although the

homolytic final product $\text{Ce}^{3+}\text{-OH}/\text{Ce}^{3+}\text{-OH}$ is energetically very favorable, 2-3 eV exothermic with respect to the reactants initial energy. Very recently, H_2 dissociation was also investigated on other CeO_2 surfaces^{36,38} and it was found that the surface termination plays a key-role on both the activation energy and the stabilization of the heterolytic product. However, the homolytic product reminds systematically the most stable one, disfavoring the presence of hydride species at the surface.^{33,34,36,38}

Previous work of Vecchiotti et al.³⁹ report the formation of Ce-H hydride species as a key step in the semi-hydrogenation of alkyne. Moreover, Vilé et al.²⁸ and Carrasco et al.²⁹ have shown that the presence of oxygen vacancy was detrimental to the alkyne hydrogenation. Because Ce_2O_3 surfaces are expected to have a non-reducible character⁴⁰, on the one hand, the heterolytic product will be favored over the homolytic one^{41,42} leading to the stabilization of surface hydrides. On the other hand the formation of oxygen vacancy is expected to be significantly less favorable than on CeO_2 surfaces. In this context, Ce_2O_3 appears like a very promising catalyst for semi-hydrogenation of alkyne, and more generally for all kind of hydrogenation reaction.

Herein, we provide in a first part a structural description of the most stable A- Ce_2O_3 surfaces and propose a structure-stability relationship. Then, the non-reducible character of A- Ce_2O_3 bulk and surfaces will be investigated by means of the oxygen vacancy formation energy descriptor. And finally, we report for the first time the study of H_2 dissociation on A- Ce_2O_3 surfaces with unexpected and extremely low activation energies.

2. Methodology

2.1. Computational details

All the calculations are computed within the Density Functional Theory (DFT) as implemented in the Vienna Ab initio Simulation Package (VASP) program, version 5.4.4.⁴³⁻⁴⁶ Projector-Augmented

Wave^{47,48} (PAW) pseudopotentials were used to describe the core electrons. Kullgren et al.⁴⁹ have shown that both standard and soft pseudopotentials of oxygen yielded to a correct description of Ce₂O₃. Moreover, Skorodumova et al.⁵⁰ showed that the localized 4*f* electrons in Ce₂O₃ can be modeled by a core state model (CSM), i.e. by treating the 4*f* electrons as a part of the core electrons. Thus, the following PAW pseudopotentials were used: trivalent pseudopotential for cerium (i.e. with 4*f* electron kept frozen in the core), soft one for oxygen and standard pseudopotential for hydrogen. Regarding the valence electrons (i.e. Ce: 5s²5p⁶5d¹6s²; O: 2s²2p⁴ and H: 1s¹), they were expanded in a plane waves basis set with kinetic energy cutoff of 300 eV. The Perdew-Becke-Ernzerhof (PBE) functional^{51,52} was used. Total energies were converged to 10⁻⁵ eV in the self-consistent field and structures were relaxed using a conjugate-gradient algorithm until the Hellmann-Feynman forces acting on each atom were lower than 10⁻² eV/Å. Spin-polarized calculation were carried out for the homolytic product (OH,OH). This computational scheme leads to excellent agreement for optimized bulk parameters, intermediate species stability and oxygen vacancy formation energy, see below and Table S1.

To find transition states, a two-step protocol was followed. First, the Climbing Image Nudged Elastic Band^{53,54} (CI-NEB) algorithm including at least five images along the reaction coordinates was used in order to get a good guess of the transition state, typically after 150 iterations. Then, the Improved Dimer Method^{55,56} (IDM) was employed to climb up to the stationary point. The nature of all the transition states (TS) was confirmed by performing a frequency analysis using the numerical Hessian matrix obtained in the framework of finite difference method with atomic displacement of 0.015 Å. The eigenvector of the imaginary frequency was checked to lead to initial and final states.

The Infrared (IR) spectra were computed in the Density Functional Perturbation Theory (DFPT) framework⁵⁷. The intensity of the vibrational modes was calculated in the dipole approximation and was extended in a terms of Born Effective Charge (BEC) and displacement vectors⁵⁸:

$$I(\sigma) = \sum_{\alpha=1}^3 \left| \sum_{i=1}^N \sum_{\beta=1}^3 Z_{\alpha\beta}^*(i) e_{\beta}(i) \right|^2$$

where $I(\sigma)$ is the intensity of the vibrational mode σ , α and β represent the cartesian polarizations, i denotes the atoms, $Z_{\alpha\beta}^*(i)$ is the BEC tensor of the i^{th} atoms and $e_{\beta}(i)$ its normalized eigenvector of the σ^{th} mode.

2.2. Surface models

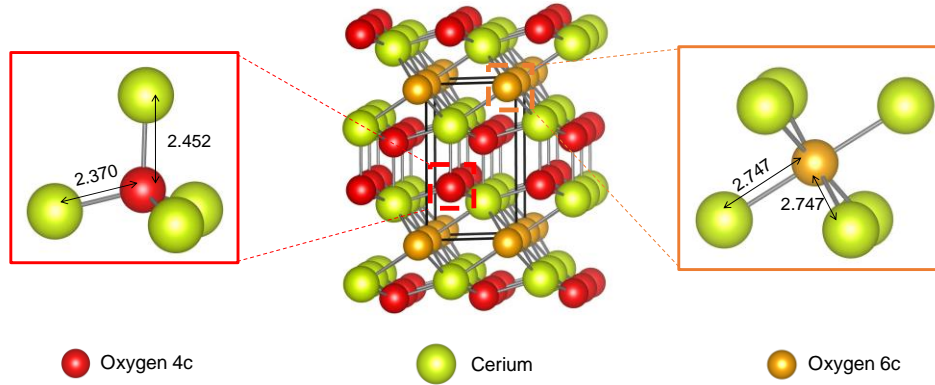


Fig. 1 Crystalline structure of A-Ce₂O₃ bulk. Cerium and oxygen 4-fold (O4c) and 6-fold (O6c) coordinated atoms are depicted by yellow, red and orange balls, respectively.

The cerium sesquioxide Ce₂O₃ A-type structure (hexagonal space group: $P\bar{3}m1$) is the most stable phase under standard conditions^{10,26,49,59,60}. In this crystalline structure depicted in Fig. 1, the two cerium atoms are seven-fold coordinated while two of the oxygen atoms are four-fold coordinated and the third one is six-fold coordinated, labeled as O4c and O6c, respectively. The optimized lattice parameters of A-Ce₂O₃ using a Monkhorst–Pack⁶¹ 15x15x8 k-point grid are in good agreement with experimental values^{62,63} and previous theoretical studies^{10,49,50,64–70} (Table 1).

	a	c	u _{Ce}	u _O	d _{Ce-O}	Ref.
PBE ^a	3.94	6.19	0.248	0.644	3 x 2.37; 1 x 2.45; 3 x 2.75	This work

PW91 ^a	3.97	6.15				50
HSE ^b	3.87	6.07	0.246	0.646		69
PBE+U ^b	3.92	6.18	0.247	0.645		10
Exp.	3.89	6.06	0.245	0.647	3 x 2.34 ; 1 x 2.43 ; 3 x 2.69	62,63

Table 1. Bulk properties of the A-Ce₂O₃ structure: a and c are the cell parameters (Å), u_{Ce} and u_O are the internal parameters and d_{Ce-O} is the distance cerium – oxygen (Å).

^a PAW calculation with the Ce 4f states in the core shell.

^b PAW calculation with the Ce 4f states in the valence shell.

The optimized bulk structure was used to build the slab models. In a first step, the surfaces were fully optimized, i. e. all the atoms were allowed to relax. Thus, the symmetry of the slabs is preserved, and the surface energy is calculated to evaluate the relative stability of the surfaces. Then, the bottom half slab was frozen for the study of vacancy formation and H₂ dissociation. We have investigated low Miller indices surfaces and retain the four most stables: (0001), (01-11), (11-20) and (11-21) (Fig. 2). All the surface models considered are non-polar, terminated so as to minimize the number of dangling bonds left with respect to the bulk within the orientation chosen, and contain enough atomic layers to converge the surface energy within 10⁻² J/m² (see Supporting Information). A vacuum layer of at least 15 Å thickness was introduced to avoid interactions between slabs. The properties (size, composition, atom coordination) as well as the computational settings (Monkhorst–Pack k-point grid and frozen atomic layers) of the four surface models are given in Table 2.

3. Results and discussion

3.1. Bare slabs

From a structural point of view, surfaces of high symmetry can be distinguished from surfaces showing a low symmetry level. (0001) and (11-20) terminations belong to the high symmetry class with only one surface Ce type and one and two surface O sites, respectively. (01-11) and (11-21) are low symmetry surfaces with two inequivalent surface Ce sites and two and three surface O sites, respectively. Moreover, the four surfaces differ also from the coordination number of their surface sites (Table 2). Indeed, depending of the termination considered, Ce and O surface sites can be 5 and/or 6-fold coordinated and 3 and/or 4-fold coordinated, respectively.

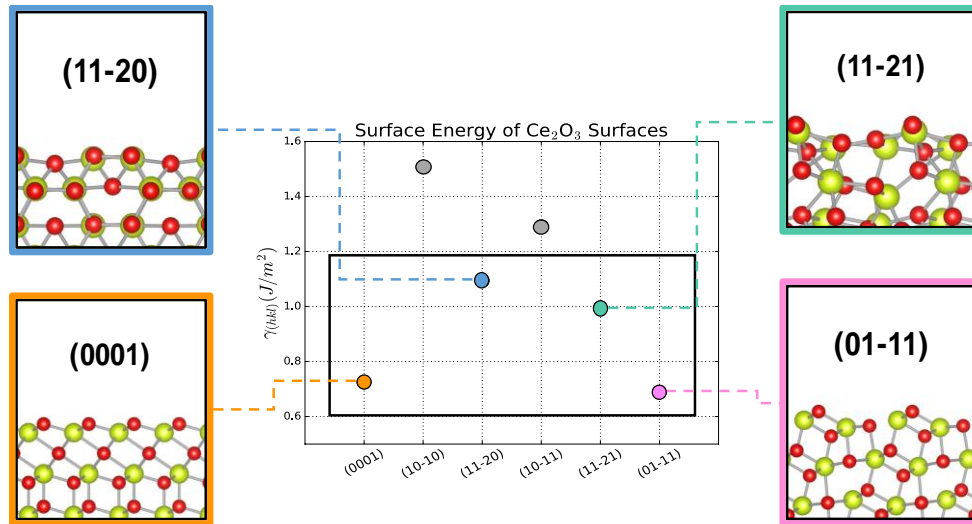


Fig. 2 Surface energy (in J/m^2) of the low Miller indices surfaces of Ce_2O_3 and side view of the structure for the four most stable surfaces.

The stability of the bare surfaces was investigated by means of the surface energy calculated as:

$$\gamma_{hkl} = \frac{E_{\text{slab},hkl} - NE_{\text{bulk}}}{2A_{hkl}}$$

where $E_{\text{slab},hkl}$ is the energy of the (hkl) supercell, N the number of Ce_2O_3 bulk unit in the supercell, E_{bulk} the reference energy of one bulk unit and A_{hkl} the surface area of the supercell.

The stability trend of the studied surfaces is: $(11-20) < (11-21) < (0001) < (01-11)$. A relationship between the surface stability and the coordination number of surface sites was found. Indeed, it appears that the

lower the coordination number of both Ce and O surface sites, the higher the surface energy (Table 2), and thus the lower surface stability.

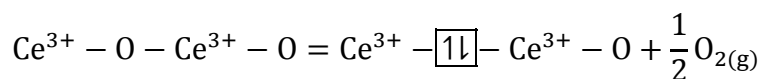
	(0001)	(01-11)	(11-20)	(11-21)
supercell	3x3	4x2	2x2	2x2
lattice constants (Å)	a = b = 11.828	a = 15.770 b = 14.686	a = 12.389 b = 13.657	a = 13.657 b = 14.686
composition (Ce ₂ O ₃ units)	27	40	28	36
atomic layers (frozen/relaxed)	15 (8/7)	25 (13/12)	7 (4/3)	45 (22/23)
area (nm ²)	1.21	2.23	1.69	1.78
k-point grid	2x2x1	1x1x1	2x1x1	2x2x1
coordination number of surface sites	Ce(6) O(3)	Ce(6) O(3; 4)	Ce(5) O(3; 4)	Ce(5; 6) O(3; 4)
γ_{hkil} (J/m ²)	0.73	0.69	1.09	1.02

Table 2. Size, lattice constants (in Å), composition (in Ce₂O₃ units), number of atomic layers, area (in nm²), k-point grid and surface energies (in J/m²) of the slab models as well as coordination number of surface sites.

3.2. Oxygen vacancy

Bulk

The formation of oxygen vacancy in Ce₂O₃ was investigated by removing one oxygen located in the bulk or at the (sub)surface:



The energy cost of the formation of this vacancy was calculated according to:

$$E_{\text{form}}^{\text{OV}} = \frac{1}{N_{\text{OV}}} \left(E_{\text{bulk/slab,OV}} - E_{\text{bulk/slab}} - N_{\text{OV}} \times \frac{1}{2} E_{\text{O}_2(\text{g})} \right)$$

where N_{OV} is the number of oxygen vacancy, $E_{\text{form}}^{\text{OV}}$ is the formation energy of oxygen vacancy, $E_{\text{bulk/slab,OV}}$ the energy of the bulk or slab with the vacancy, $E_{\text{bulk/slab}}$ the energy of the free-defect bulk or slab, and $E_{\text{O}_2(\text{g})}$ the energy of O_2 molecule in gas phase (-9.28 eV, not corrected).

In the bulk, the formation of oxygen vacancy was investigated by considering one and two defects in the 2x2x2 and 3x3x3 supercells, corresponding to oxygen defect rate of $\theta = \left\{ \frac{1}{24}, \frac{1}{12}, \frac{1}{81}, \frac{2}{81} \right\}$. For one oxygen vacancy, the defects of four and six-fold coordinated oxygens were considered and results in the study of 2 configurations (one for O4c and one for O6c) for both 2x2x2 and 3x3x3 supercells. In the case of two oxygen vacancies, the problem is more complex: removing two oxygen leads to 276 and 3240 configurations for the 2x2x2 and 3x3x3 supercells, respectively. However, by taking into account the symmetry operations of the crystal, this reduces to 14 and 30 irreducible configurations for 2x2x2 and 3x3x3, respectively. All the possibilities were explored. For 2x2x2 and 3x3x3 supercell, the most stable configuration is found for neighboring O6c vacancies along [010] and [110] directions, respectively (see Figure S6).

Contrary to CeO_2 where the formation of an oxygen vacancy lead to the reduction of two Ce^{4+} in Ce^{3+} , removing one oxygen in Ce_2O_3 results in the formation of a vacancy filled by two electrons, also called F^0 center (Fig. 3 and Fig. 5). The generation of an F^0 center after removing an oxygen from the structure is characteristic of non-reducible oxides.⁴⁰ From an electronic point of view, the formation of oxygen defect in Ce_2O_3 bulk is characterized by the appearance of a narrow band located around 5.5 eV, resulting in a shift of the Fermi energy of +2.8 eV compared to the stoichiometric composition (Fig. 3). The Projected Density Of States (PDOS) indicates a very small contribution of cerium and oxygen atoms to the highest occupied band, which is characteristic of F^0 center. Moreover, the isosurface of this band, as depicted in

Fig. 3, confirms the formation of an F^0 center located on the oxygen vacancy. However, the PDOS shows that the position and the width of the bands as well as their atomic contributions are not modified when the oxygen defect are introduced (Fig. 3). This indicates that the electrostatic interactions between the F^0 center and the neighboring Ce^{3+} cations tend to restore a bulk-like free defect configuration.

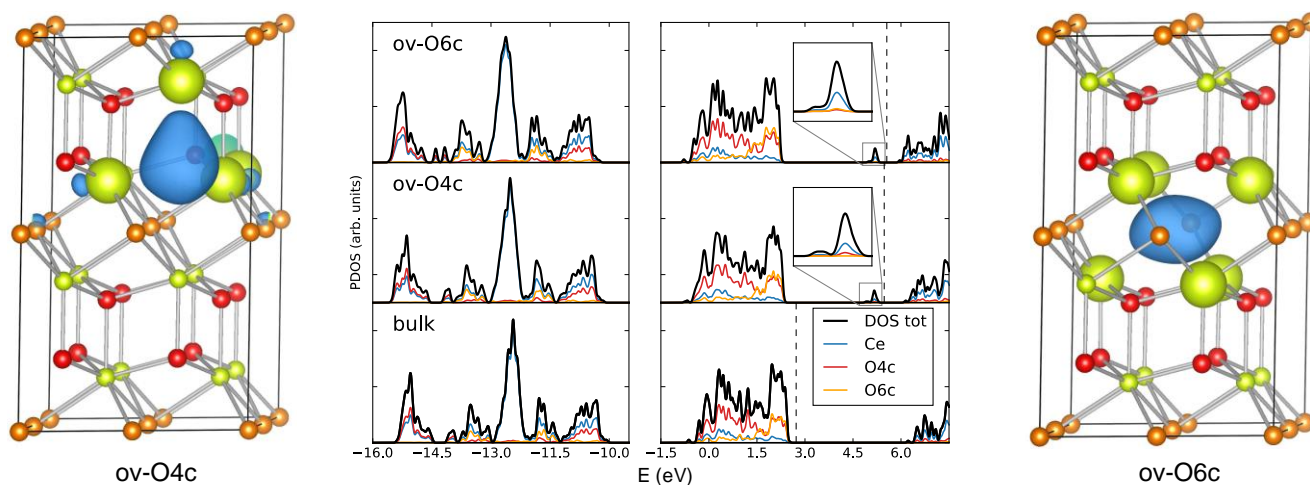


Fig. 3 PDOS of bulk, O4c and O6c oxygen vacancies in $2 \times 2 \times 2$ - Ce_2O_3 bulk as well as the isosurface of the highest occupied band corresponding with a F^0 center located on the oxygen defect. The Fermi energy is depicted by a dashed line. Cerium bound to the oxygen defect are represented by large balls while all the other atoms are depicted with small balls for the sake of clarity.

The non-reducible character of Ce_2O_3 is also confirmed by the large energy required to form an oxygen vacancy, i.e. > 5 eV (Table 3). The stability of F-centers has also been observed in other poorly reducible oxides⁷¹, and is associated to a high coordination stabilized by electrostatic interaction with neighboring cations. Two main effects account for the value of the formation energy of oxygen vacancy. First, the relaxation, which is usually very small because the electrostatics maintains the structure around the two electrons left, and second, the coordination of the oxygen site, which plays two opposite roles. Indeed, on the one hand, the neighboring cations will stabilize the final product i.e. the electrons left, by means of electrostatic interactions, and thus the formation energy tends to decrease. But on the other hand, a high

number of neighbors involves many bonds to be broken, thus a higher formation energy value. In the case of Ce_2O_3 , the formation energy of O4c vacancy is higher than the one for O6c vacancy type. This could indicate that the electrostatic effect is predominant and governs the stability of the oxygen defect.

	1xOV		2xOV		
	O4c	O6c	2xO4c	2xO6c	O4c + O6c
2x2x2	6.47	6.24	6.41 – 6.51	6.23 – 6.28	6.25 – 6.35
3x3x3	6.47	6.21	6.44 – 6.49	6.19 – 6.24	6.30 – 6.34

Table 3. Formation energy (in eV) of oxygen vacancy in bulk for 2x2x2 and 3x3x3 supercell.

Moreover, it was found that the formation energy is strictly independent of the oxygen defect concentration (from $\theta = \frac{1}{12}$ to $\theta = \frac{1}{81}$), confirming that the oxygen defect in Ce_2O_3 is mainly governed by electrostatic interactions between F^0 centers and Ce^{3+} cations. More interesting, in the case of two oxygen vacancies, the formation energy is equal to the average of the two isolated vacancies:

$$E_{\text{form}}^{2 \times \text{OV}} = \frac{1}{2} (E_{\text{form}}^{\text{OV}_1} + E_{\text{form}}^{\text{OV}_2})$$

This means that if the two oxygen vacancies are of the O4c (O6c) type, then the formation energy will be equal to the formation energy of O4c (O6c) vacancy, and if one of the oxygen vacancies is of the O4c type and the other of the O6c type, then the formation energy will be the average of the O4c and O6c defects (Fig. 4).

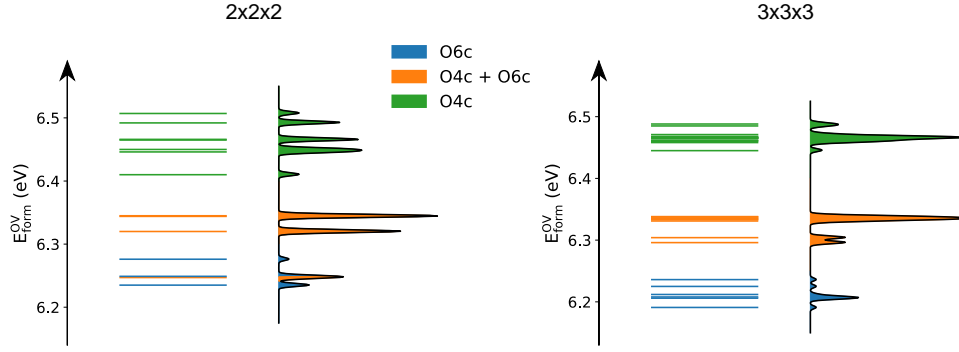


Fig. 4 Formation energies (in eV) of two oxygen vacancies for 2x2x2 (left) and 3x3x3 (right) in Ce_2O_3 bulk supercells. The degeneracy of the oxygen vacancies configurations is also represented. The most stable configurations are given in Supporting Information and correspond to neighboring O6c vacancies along [010] and [110] directions for 2x2x2 and 3x3x3, respectively.

Surface

Regarding the formation of oxygen vacancy on Ce_2O_3 surfaces, a bulk-like behavior is observed with the formation of F^0 center (Fig. 5). The DOS of the oxygen vacancy is similar to the bulk one and is given in the Supplementary Information. For the (01-11), (11-20) and (11-21) terminations which have non-equivalent (sub)surface oxygen sites, all the different oxygen vacancies configuration were investigated and their formation energies were summarized in Table 4. Moreover, the large formation energy of such defect (> 5.5 eV) indicates that the surfaces retain the non-reducible character of the bulk. These results suggest a lower density of oxygen defects on Ce_2O_3 surfaces compared to CeO_2 where the formation of oxygen vacancy is of the order of $1.5 - 2.5 \text{ eV}^{72-74}$, depending on the termination.

	(0001)	(01-11)	(11-20)	(11-21)
$E_{\text{form}}^{\text{SOV}}$	6.51	5.73 / 6.00	5.20 / 5.15	5.50 / 5.74 / 5.82
$E_{\text{form}}^{\text{SSOV}}$	5.94	6.11	5.20 / 5.80	5.49 / 5.48 / 6.17 / 6.30
$\gamma_{\text{hkil}} (\text{J/m}^2)$	0.73	0.69	1.09	1.02

Table 4. Formation energy of surface (SOV) and subsurface (SSOV) oxygen vacancies (in eV) as well as surface energies (in J/m²). The structures related to the oxygen vacancy formation energy are given in Supporting Information.

Furthermore, we can note that the energy cost increases inversely with the stability of the surfaces. This can be explained by the relationship between the surface stability and its reactivity. Indeed, a stable termination tends to be more inert – and so less reactive – than other less stable surfaces. It can be seen from Table 4 that the (01-11), (11-20) and (11-21) terminations display similar formation energy values for surface and subsurface sites, indicating a similar stabilization of the O-defective system. However, the (0001) termination shows the opposite behavior, indicating that the local environment of the vacancy in the subsurface position is more stabilizing for the vacancy. In other words, there is a trend for the (0001) termination to stabilize vacancies in more inner positions, probably favoring the migration of vacancies to the bulk. It is worth noting that from a structural point of view, the (0001) surface is very similar to the CeO₂ (111) termination²⁷ (see Figure S8). Indeed, both show an hexagonal structure and similar experimental lattice constants: 3.89 and 3.88 Å for (0001)-Ce₂O₃ and (111)-CeO₂, respectively. Moreover, in CeO₂, the (111) surface is the only one where the subsurface oxygen vacancy is also expected to be more stable than the surface one.⁷⁴

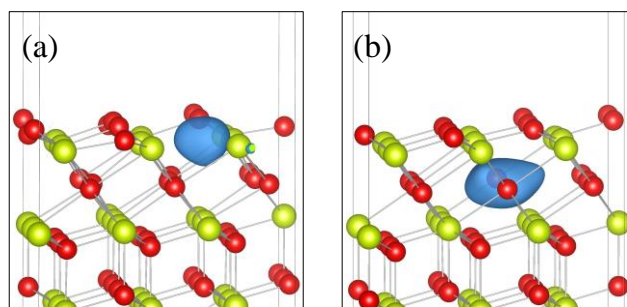
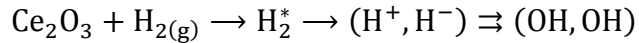


Fig. 5 Relaxed structure and isosurface of the band related to the F⁰ center located on the defect for (a) surface vacancy (6.51 eV) and (b) subsurface oxygen vacancy (5.94 eV) for (0001) surface.

3.3. H₂ dissociation

The heterolytic dissociation of H₂ molecule on Ce₂O₃ surfaces leads to the formation of a proton/hydride pair, bound to Ce and O sites, respectively. In the following, the heterolytic product will be labeled (H⁺,H⁻). For the surfaces showing different O and/or Ce surface sites, all the (H⁺,H⁻) were investigated but only the most stable one was reported. Moreover, the product of the homolytic dissociation – labeled as (OH,OH) – was also considered in order to check if the heterolytic product is susceptible to evolve toward the homolytic one, as observed in CeO₂.^{33,34,38} So, in this study, the following reaction pathway was considered:



where Ce₂O₃ and H₂ represent the bare slabs and H₂ molecule in gas phase, H₂^{*} as the physisorbed molecule, (H⁺,H⁻) and (OH,OH) represent the heterolytic and homolytic products, respectively.

Energetic profile

All adsorption energies were referenced to the H₂ molecule in the gas phase and the bare slabs and were calculated as:

$$E_{\text{ads}}^i = E_{\text{slab},i} - E_{\text{slab}} - E_{\text{H}_2(\text{g})}$$

where E_{ads}^i is the adsorption energy of i species, $E_{\text{slab},i}$ the energy of the slab with i , E_{slab} the energy of the slab and $E_{\text{H}_2(\text{g})}$ the energy of hydrogen molecule in gas phase.

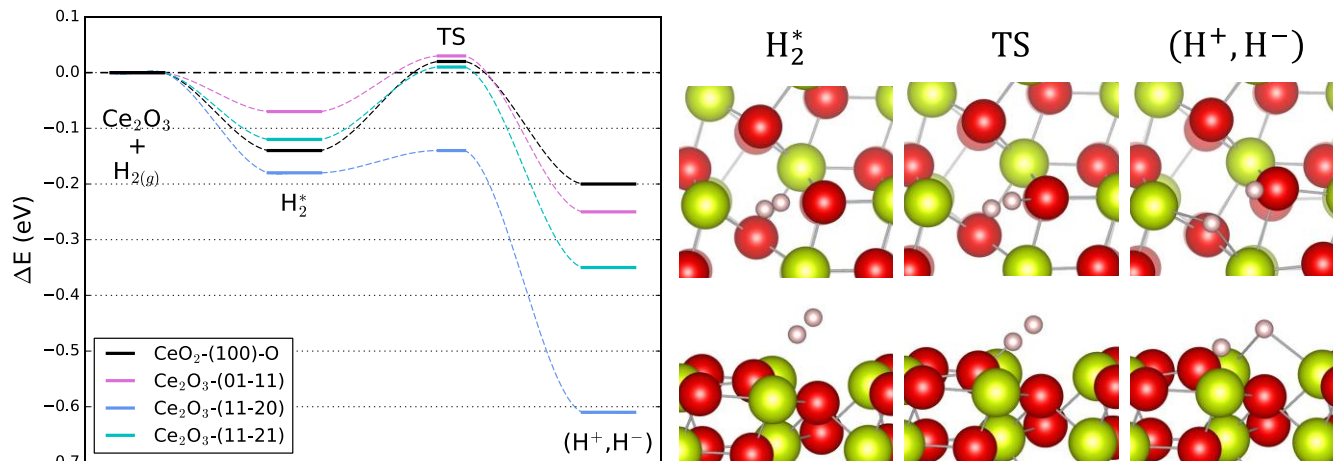


Fig. 6 At left: energetic profile (in eV) for the heterolytic dissociation of H_2 molecule on Ce_2O_3 surfaces. The energetic profile for the CeO_2 surface (100)-O terminated is taken from ref.³⁸ At right: top and side view of H_2^* , TS and (H^+, H^-) species on (11-20) surface.

The energetic profile of the dissociation is depicted in Fig. 6 and is summarized in Table 5. The nature of hydride and proton species was confirmed by a Bader charge analysis.^{75–78} For all the surfaces studied, the weak adsorption of H_2 molecule indicates the physisorption nature of this first step. For the (0001) termination, we did not find any (H^+, H^-) species. This could be due to (i) no minimum on the potential surface energy correspond with the (H^+, H^-) species or (ii) the potential surface energy is very smooth around the local minimum corresponding to (H^+, H^-) rendering the conjugate-gradient algorithm inefficient to locate the minimum. In order to have an idea on the stability of such species on (0001) termination, we have considered the configuration where the hydride and proton species are far and away, i.e. not on neighboring oxygen and cerium sites, to prevent recombination as H_2 during optimization. The corresponding (H^+, H^-) pair was found to be endothermic of +0.97 eV. For all the others surfaces, the (H^+, H^-) product is thermodynamically stable, i.e. with negative adsorption energies. This indicates that Ce_2O_3 stabilizes the heterolytic product compared to CeO_2 who tends to lead to an unstable (H^+, H^-) product.^{33,34,38} Furthermore, the activation energy of the dissociation is very low, from 0.04 eV for (11-20)

to 0.13 eV for (11-21). Thus, the H₂ dissociation is expected to be very favorable on Ce₂O₃ surfaces, in contrast with CeO₂ where the activation energy is still significantly larger (although dependent of structure of the termination³⁸). Moreover, the energetic profile of H₂ dissociation is smooth (i.e. with energy differences in the range of |0.28| and |0.47| eV between transition structures and final states). This means that Ce₂O₃ surfaces are good candidates to split H₂ because the required activation energy is very low, and they do not over stabilize the product. However, for the (01-11) and (11-21) surfaces, the slight endothermicity (-0.25 and -0.35 eV, respectively) of the heterolytic product (H⁺,H⁻) indicates that it can easily desorb back as H₂ molecule.

	(0001)	(01-11)	(11-20)	(11-21)
H ₂ [*]	-0.04	-0.07	-0.18	-0.12
TS	/	0.03	-0.14	0.01
(H ⁺ ,H ⁻)	0.97 ^(a)	-0.25	-0.61	-0.35
(OH,OH)	2.86	1.92	0.85	1.06

Table 5. Adsorption energies (in eV) of the species involved in the H₂ dissociation process. ^(a) The hydride and proton species are far and away ($d_{\text{H}^+-\text{H}^-} = 5.927 \text{ \AA}$).

Finally, we can note that the homolytic product (OH,OH) in Ce₂O₃ leads to two electrons left in the surface due to the non-reducibility of Ce³⁺ cations, contrary to CeO₂ surfaces where it gives rise to the reduction of two Ce⁴⁺ ^{33,34,38}. The Bader charge analysis as well as the PDOS of (OH,OH) species indicate that these two electrons are mainly localized on the oxygens bound to the hydrogen atoms and on the cerium previously involved in Ce-H⁻ bond. The homolytic product is on the one hand much less stable than the heterolytic product (H⁺,H⁻) and on the other hand strongly endothermic. These results argue in favor of the stabilization of hydride species on Ce₂O₃ surfaces. It is important to note that on CeO₂, the H₂ dissociation occurs according to an heterolytic mechanism, like Ce₂O₃, but leads to homolytic product due to the strong exothermicity of (OH,OH). The differences of behavior between

CeO₂ and Ce₂O₃ can be explained by the reducible and non-reducible character of these metal oxides. Indeed, while reducible metal oxide like CeO₂ promotes the homolytic product, an irreducible oxide as Ce₂O₃ favors the heterolytic pathway and product. Poorly reducible oxides like MgO⁷⁹⁻⁸¹ or ZrO₂⁸² are also found to stabilize surface hydride species.

To summarize, Ce₂O₃ surfaces show two interesting advantages over CeO₂: they allow to dissociate H₂ with an extremely low activation energy, and favor the hydride species by avoiding the evolution of (H⁺,H⁻) toward (OH,OH).

Electronic structure

From an electronic point of view, the H₂ dissociation mechanism on Ce₂O₃ surfaces is independent of the terminations and the electronic transfers are well identified. Because all the surfaces studied display a similar behavior, only the PDOS of the different step of H₂ dissociation for (01-11) termination were depicted in Fig. 7, where only the projections of Ce–H and O–H atoms were depicted for the sake of clarity. The PDOS of the other surfaces are given in Supplementary Information. First, the physisorption of H₂ is characterized by the appearance of a narrow band around -7.2 eV which is typical of H₂ molecule. Then, for TS, the electron transfer from H^{δ+} to H^{δ-} is initiated with the rise of the H₂ band splitting. Indeed, we can observe the appearance of a wide band just below the Fermi energy associated to hydride species while the remaining H₂ band around -6.8 eV is related to proton species. Finally, the formation of heterolytic product (H⁺,H⁻) marks the end of the electronic transfer with two well defined bands around -6.8 eV and -1.0 eV associated to formal proton and hydride species, respectively. Regarding the homolytic product (OH,OH), the two electrons coming from H₂ molecule are well localized in the narrow band around +2.0 eV. The appearance of this band filled by the two electrons has for consequence to shift the Fermi energy to +3.0 eV compared to the heterolytic product (H⁺,H⁻). This can

explain the endothermicity of (OH,OH) and why such species are expected to be unstable on Ce_2O_3 surfaces.

During the heterolytic dissociation, the Fermi energy is not or slightly shifted (i.e. < 0.1 eV), and this for all the terminations studied. Similar observations were reported for low activation energy of H_2 molecule on CeO_2 surfaces.³⁸ More precisely, we found that the bands related to the TS and (H^+, H^-) are overlapping with the slab bands (Fig. 7). Interestingly, previous work of Santos et al.⁸³ reported that this overlap is associated to a lower activation energy for the hydrogen evolution reaction in metals. Thus, the overlapping between heterolytic product and slab bands could be an indicator for the stability of product and the activation energy: stable product and low activation energy are expected in the presence of such overlapping while its absence leads to unstable product and higher energetical barrier.

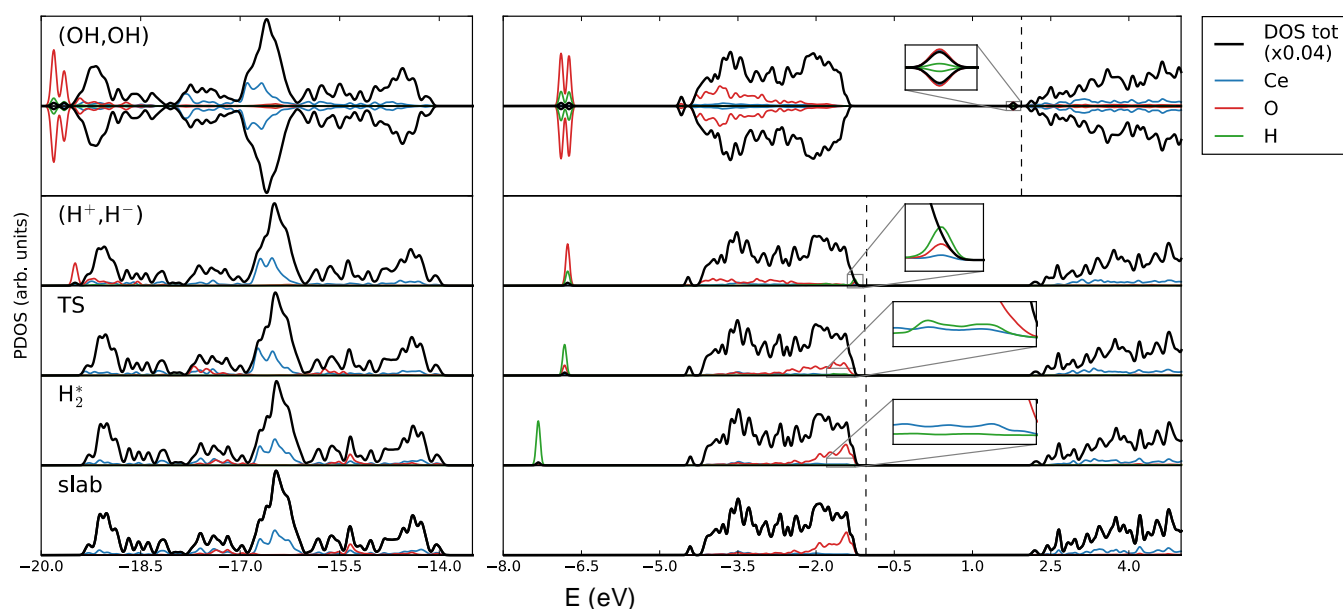


Fig. 7 DOS (x0.04) of slab, H_2^* , TS, heterolytic product (H^+, H^-) and homolytic product (OH, OH) for (01-11) surface. PDOS (x1.00) of atoms directly involved in the H_2 dissociation process, i.e. oxygen and cerium bound to hydrogen atoms, are also represented. The cerium, oxygen and hydrogen PDOS are depicted by blue, red and green lines, respectively and the Fermi energy is represented by dashed lines.

Infrared spectra

The Infrared spectra were computed for all the (H^+,H) species using the same methodology presented in our previous work³⁸. Vibrational region of hydrogen species on reduced cerium oxide Ce_2O_3 are similar to the ones found for oxidized ceria CeO_2 with the distribution of the wavenumbers in three regions (Fig. 8): the bending modes of Ce–H and O–H are characterized by low frequencies (550 – 900 cm^{-1}); Ce–H and O–H stretching modes show higher frequencies in the region of 900 – 1200 cm^{-1} and 2600 – 3600 cm^{-1} , respectively. For the (01-11) surface, the red shift observed in the O–H stretching is not due to hydrogen bond but to the non-zero interaction between the two hydrogens atoms ($d_{H+H} = 1.412 \text{ \AA}$). Moreover, the Ce–H stretching mode on Ce_2O_3 is shifted to lower wavenumbers compared to CeO_2 . This expected redshift for the Ce–H stretching vibration can be explained by the observation of larger bond length distances between Ce and H in Ce_2O_3 ($d_{Ce-H} \sim 2.5 \text{ \AA}$ compared to $\sim 2.2 \text{ \AA}$ in CeO_2).

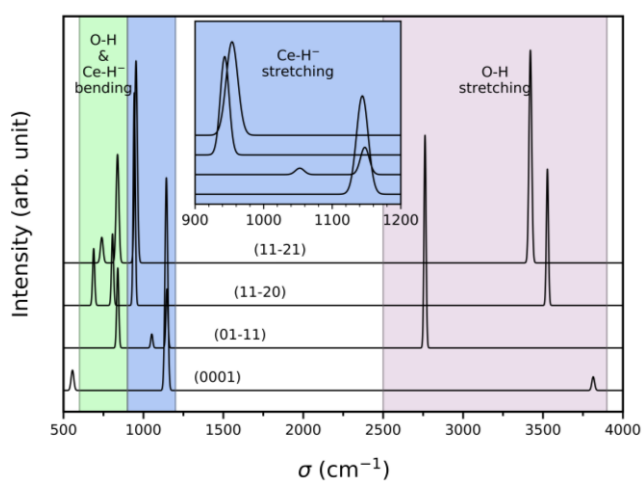


Fig. 8 Computed Infrared Spectra of the dissociation product (H^+,H) for the four surfaces studied. For the (0001) termination, the spectra is given for the structure where the hydride and proton are far and away. Intensities are given in arbitrary units. A gaussian broadening of 15 cm^{-1} width is applied on the intensities.

Interestingly, the intensities of vibrations involving hydrides are expected to be important (Table 6) and contrary to CeO₂, hydrides on Ce₂O₃ are both thermodynamically stabilized and more stable than the homolytic product. These results suggest that the observation of hydrides is much more probable on Ce₂O₃ and enable the characterization of this species with IR spectroscopy.

	(0001) ^(a)	(01-11)	(11-20)	(11-21)
$\nu_{\text{Ce-H}}^{\text{stretch}}$	1144.0 (1.00)	1147.6 (0.28)	943.2 (1.00)	953.9 (0.95)
$\nu_{\text{O-H}}^{\text{stretch}}$	3814.5 (0.06)	2762.3 (1.00)	3528.0 (0.64)	3421.3 (1.00)

Table 6. Wavenumbers (in cm⁻¹) and their Infrared intensities (in arbitrary unit) in brackets for Ce–H and O–H vibrational stretching modes for (H⁺,H⁻) species on (0001), (01-11), (11-20) and (11-21) surfaces.

^(a) Hydride and proton are far away

4. Conclusion

In summary, this work provides a detailed description of the four most stable surfaces of A-Ce₂O₃ and investigated the reactivity of these surfaces by considering H₂ dissociation and oxygen vacancy formation. The former shows important features in catalytic field, in particular in semi-hydrogenation of alkyne, the latter one provides precious information about the non-reducible character of Ce₂O₃.

Compared to CeO₂, the complete reduction of ceria (Ce₂O₃) is characterized by three major changes in the H₂ dissociation:

- (i) decreasing significantly the activation energy leading to a quasi-spontaneous reaction with an energetic barrier as low as ~0.1 eV;
- (ii) thermodynamically stabilizing surface hydride species while on stoichiometric ceria (CeO₂), this was only observed for (100) surfaces;

- (iii) favoring heterolytic product compared to homolytic one, thus promoting the stabilization of hydride more than the hydroxyl species while on CeO_2 , the inverse is observed even on partially reduced surfaces.

Moreover, our results confirm the vibrational region of surface hydride on cerium oxide in the range of 900 and 1200 cm^{-1} .

Regarding the reducibility of Ce_2O_3 , our results show that the formation of oxygen vacancy leads to the formation of F^0 center and highlight the non-reducibility of Ce_2O_3 . Moreover, our results indicate that the formation of oxygen defect in Ce_2O_3 is mainly governed by electrostatic interactions between F^0 center and Ce^{3+} cations which maintains the structure. We also found that surface oxygen vacancy is preferred to subsurface positions, except for (0001) termination where the subsurface vacancy is favored, as observed in the (111)- CeO_2 termination too.

Supporting Information

Results of the choice of the cutoff for the bulk and thickness convergence tests for all the slab model. The structures (POSCAR format) of bare slabs, TS and (H^+ ,H) minima were also given. The DOS and PDOS of oxygen vacancies as well as the different steps involved in H_2 dissociation were provided for all the surfaces.

Acknowledgements

Authors acknowledge Scienomics for the MAPS program used in the construction of the slab models for a courtesy license. Dr. B. Diawara is acknowledged for the Modelview program. This work was performed using HPC resources from GENCI- CINES/IDRIS (Grant 2018- x2018082131 and 2017- x2017082131), and the PER-SU iDROGEN project.

References

- (1) Fu, Q.; Saltsburg, H.; Flytzani-Stephanopoulos, M. Active Nonmetallic Au and Pt Species on Ceria-Based Water-Gas Shift Catalysts. *Science* **2003**, *301* (5635), 935. <https://doi.org/10.1126/science.1085721>.
- (2) Deluga, G. A.; Salge, J. R.; Schmidt, L. D.; Verykios, X. E. Renewable Hydrogen from Ethanol by Autothermal Reforming. *Science* **2004**, *303* (5660), 993. <https://doi.org/10.1126/science.1093045>.
- (3) Shao, Z.; Haile, S. M. A High-Performance Cathode for the next Generation of Solid-Oxide Fuel Cells. *Nature* **2004**, *431*, 170.
- (4) Jasinski, P.; Suzuki, T.; Anderson, H. U. Nanocrystalline Undoped Ceria Oxygen Sensor. *Sens. Actuators B Chem.* **2003**, *95* (1–3), 73–77. [https://doi.org/10.1016/S0925-4005\(03\)00407-6](https://doi.org/10.1016/S0925-4005(03)00407-6).
- (5) Trovarelli, A.; Fornasiero, P. *Catalysis by Ceria and Related Materials*, 2nd edition.; Catalytic Science Series; Imperial College Press: London, 2013.
- (6) Trovarelli, A.; de Leitenburg, C.; Boaro, M.; Dolcetti, G. The Utilization of Ceria in Industrial Catalysis. *Catal. Today* **1999**, *50* (2), 353–367. [https://doi.org/10.1016/S0920-5861\(98\)00515-X](https://doi.org/10.1016/S0920-5861(98)00515-X).
- (7) Aneggi, E.; Boaro, M.; Leitenburg, C. de; Dolcetti, G.; Trovarelli, A. Insights into the Redox Properties of Ceria-Based Oxides and Their Implications in Catalysis. *J. Alloys Compd.* **2006**, *408–412*, 1096–1102. <https://doi.org/10.1016/j.jallcom.2004.12.113>.
- (8) Lawrence, N. J.; Brewer, J. R.; Wang, L.; Wu, T.-S.; Wells-Kingsbury, J.; Ihrig, M. M.; Wang, G.; Soo, Y.-L.; Mei, W.-N.; Cheung, C. L. Defect Engineering in Cubic Cerium Oxide Nanostructures for Catalytic Oxidation. *Nano Lett.* **2011**, *11* (7), 2666–2671. <https://doi.org/10.1021/nl200722z>.
- (9) Castleton, C. W. M.; Kullgren, J.; Hermansson, K. Tuning LDA+U for Electron Localization and Structure at Oxygen Vacancies in Ceria. *J. Chem. Phys.* **2007**, *127* (24), 244704. <https://doi.org/10.1063/1.2800015>.
- (10) Da Silva, J. L. F. Stability of the Ce₂O₃ Phases: A DFT + U Investigation. *Phys. Rev. B* **2007**, *76* (19). <https://doi.org/10.1103/PhysRevB.76.193108>.
- (11) Nolan, M.; Parker, S. C.; Watson, G. W. The Electronic Structure of Oxygen Vacancy Defects at the Low Index Surfaces of Ceria. *Surf. Sci.* **2005**, *595* (1–3), 223–232. <https://doi.org/10.1016/j.susc.2005.08.015>.
- (12) Torbrügge, S.; Reichling, M.; Ishiyama, A.; Morita, S.; Custance, Ó. Evidence of Subsurface Oxygen Vacancy Ordering on Reduced CeO₂(111). *Phys. Rev. Lett.* **2007**, *99* (5), 056101. <https://doi.org/10.1103/PhysRevLett.99.056101>.
- (13) Gritschneider, S.; Reichling, M. Structural Elements of CeO₂ (111) Surfaces. *Nanotechnology* **2007**, *18* (4), 044024. <https://doi.org/10.1088/0957-4484/18/4/044024>.
- (14) Murgida, G. E.; Ganduglia-Pirovano, M. V. Evidence for Subsurface Ordering of Oxygen Vacancies on the Reduced CeO₂ (111) Surface Using Density-Functional and Statistical Calculations.

Phys. Rev. Lett. **2013**, *110* (24). <https://doi.org/10.1103/PhysRevLett.110.246101>.

(15) Duchoň, T.; Dvořák, F.; Aulická, M.; Stetsovych, V.; Vorokhta, M.; Mazur, D.; Veltruská, K.; Skála, T.; Mysliveček, J.; Matolínová, I.; et al. Ordered Phases of Reduced Ceria As Epitaxial Films on Cu(111). *J. Phys. Chem. C* **2014**, *118* (1), 357–365. <https://doi.org/10.1021/jp409220p>.

(16) Olbrich, R.; Murgida, G. E.; Ferrari, V.; Barth, C.; Llois, A. M.; Reichling, M.; Ganduglia-Pirovano, M. V. Surface Stabilizes Ceria in Unexpected Stoichiometry. *J. Phys. Chem. C* **2017**, *121* (12), 6844–6851. <https://doi.org/10.1021/acs.jpcc.7b00956>.

(17) Gordon, W. O.; Xu, Y.; Mullins, D. R.; Overbury, S. H. Temperature Evolution of Structure and Bonding of Formic Acid and Formate on Fully Oxidized and Highly Reduced CeO₂(111). *Phys. Chem. Chem. Phys.* **2009**, *11* (47), 11171. <https://doi.org/10.1039/b913310k>.

(18) Mullins, D. R.; Albrecht, P. M.; Calaza, F. Variations in Reactivity on Different Crystallographic Orientations of Cerium Oxide. *Top. Catal.* **2013**, *56* (15–17), 1345–1362. <https://doi.org/10.1007/s11244-013-0146-7>.

(19) Wu, X.-P.; Gong, X.-Q.; Lu, G. Role of Oxygen Vacancies in the Surface Evolution of H at CeO₂ (111): A Charge Modification Effect. *Phys Chem Chem Phys* **2015**, *17* (5), 3544–3549. <https://doi.org/10.1039/C4CP04766D>.

(20) Kumari, N.; Haider, M. A.; Agarwal, M.; Sinha, N.; Basu, S. Role of Reduced CeO₂ (110) Surface for CO₂ Reduction to CO and Methanol. *J. Phys. Chem. C* **2016**, *120* (30), 16626–16635. <https://doi.org/10.1021/acs.jpcc.6b02860>.

(21) Zhao, C.; Xu, Y. Simulated Temperature Programmed Desorption of Acetaldehyde on CeO₂(111): Evidence for the Role of Oxygen Vacancy and Hydrogen Transfer. *Top. Catal.* **2017**, *60* (6–7), 446–458. <https://doi.org/10.1007/s11244-016-0703-y>.

(22) Ghoshal, T.; Fleming, P. G.; Holmes, J. D.; Morris, M. A. The Stability of “Ce₂O₃” Nanodots in Ambient Conditions: A Study Using Block Copolymer Templated Structures. *J. Mater. Chem.* **2012**, *22* (43), 22949. <https://doi.org/10.1039/c2jm35073d>.

(23) Hamm, C. M.; Alff, L.; Albert, B. Synthesis of Microcrystalline Ce₂O₃ and Formation of Solid Solutions between Cerium and Lanthanum Oxides. *Z. Für Anorg. Allg. Chem.* **2014**, *640* (6), 1050–1053. <https://doi.org/10.1002/zaac.201300663>.

(24) Merrifield, R. C.; Arkill, K. P.; Palmer, R. E.; Lead, J. R. A High Resolution Study of Dynamic Changes of Ce₂O₃ and CeO₂ Nanoparticles in Complex Environmental Media. *Environ. Sci. Technol.* **2017**, *51* (14), 8010–8016. <https://doi.org/10.1021/acs.est.7b01130>.

(25) Nadaroglu, H.; Onem, H.; Alayli Gungor, A. Green Synthesis of Ce₂O₃ NPs and Determination of Its Antioxidant Activity. *IET Nanobiotechnol.* **2017**, *11* (4), 411–419. <https://doi.org/10.1049/iet-nbt.2016.0138>.

(26) Höcker, J.; Krisponeit, J.-O.; Schmidt, T.; Falta, J.; Flege, J. I. The Cubic-to-Hexagonal Phase Transition of Cerium Oxide Particles: Dynamics and Structure. *Nanoscale* **2017**, *9* (27), 9352–9358. <https://doi.org/10.1039/C6NR09760J>.

- (27) Xiao, W.; Guo, Q.; Wang, E. G. Transformation of CeO₂ (111) to Ce₂O₃ (0001) Films. *Chem. Phys. Lett.* **2003**, *368* (5–6), 527–531. [https://doi.org/10.1016/S0009-2614\(02\)01889-4](https://doi.org/10.1016/S0009-2614(02)01889-4).
- (28) Vilé, G.; Bridier, B.; Wichert, J.; Pérez-Ramírez, J. Ceria in Hydrogenation Catalysis: High Selectivity in the Conversion of Alkynes to Olefins. *Angew. Chem. Int. Ed.* **2012**, *51* (34), 8620–8623. <https://doi.org/10.1002/anie.201203675>.
- (29) Carrasco, J.; Vilé, G.; Fernández-Torre, D.; Pérez, R.; Pérez-Ramírez, J.; Ganduglia-Pirovano, M. V. Molecular-Level Understanding of CeO₂ as a Catalyst for Partial Alkyne Hydrogenation. *J. Phys. Chem. C* **2014**, *118* (10), 5352–5360. <https://doi.org/10.1021/jp410478c>.
- (30) Vilé, G.; Dähler, P.; Vecchiotti, J.; Baltanás, M.; Collins, S.; Calatayud, M.; Bonivardi, A.; Pérez-Ramírez, J. Promoted Ceria Catalysts for Alkyne Semi-Hydrogenation. *J. Catal.* **2015**, *324*, 69–78. <https://doi.org/10.1016/j.jcat.2015.01.020>.
- (31) Werner, K.; Weng, X.; Calaza, F.; Sterrer, M.; Kropp, T.; Paier, J.; Sauer, J.; Wilde, M.; Fukutani, K.; Shaikhtudinov, S.; et al. Toward an Understanding of Selective Alkyne Hydrogenation on Ceria: On the Impact of O Vacancies on H₂ Interaction with CeO₂ (111). *J. Am. Chem. Soc.* **2017**, *139* (48), 17608–17616. <https://doi.org/10.1021/jacs.7b10021>.
- (32) Désaunay, T.; Bonura, G.; Chiodo, V.; Freni, S.; Couzinié, J.-P.; Bourgon, J.; Ringuedé, A.; Labat, F.; Adamo, C.; Cassir, M. Surface-Dependent Oxidation of H₂ on CeO₂ Surfaces. *J. Catal.* **2013**, *297*, 193–201. <https://doi.org/10.1016/j.jcat.2012.10.011>.
- (33) García-Melchor, M.; López, N. Homolytic Products from Heterolytic Paths in H₂ Dissociation on Metal Oxides: The Example of CeO₂. *J. Phys. Chem. C* **2014**, *118* (20), 10921–10926. <https://doi.org/10.1021/jp502309r>.
- (34) Fernández-Torre, D.; Carrasco, J.; Ganduglia-Pirovano, M. V.; Pérez, R. Hydrogen Activation, Diffusion, and Clustering on CeO₂ (111): A DFT+*U* Study. *J. Chem. Phys.* **2014**, *141* (1), 014703. <https://doi.org/10.1063/1.4885546>.
- (35) Wu, Z.; Cheng, Y.; Tao, F.; Daemen, L.; Foo, G. S.; Nguyen, L.; Zhang, X.; Beste, A.; Ramirez-Cuesta, A. J. Direct Neutron Spectroscopy Observation of Cerium Hydride Species on a Cerium Oxide Catalyst. *J. Am. Chem. Soc.* **2017**, *139* (28), 9721–9727. <https://doi.org/10.1021/jacs.7b05492>.
- (36) Huang, Z.-Q.; Liu, L.-P.; Qi, S.; Zhang, S.; Qu, Y.; Chang, C.-R. Understanding All-Solid Frustrated-Lewis-Pair Sites on CeO₂ from Theoretical Perspectives. *ACS Catal.* **2018**, *8* (1), 546–554. <https://doi.org/10.1021/acscatal.7b02732>.
- (37) Dvořák, F.; Szabová, L.; Johánek, V.; Farnesi Camellone, M.; Stetsovyh, V.; Vorokhta, M.; Tovt, A.; Skála, T.; Matolínová, I.; Tateyama, Y.; et al. Bulk Hydroxylation and Effective Water Splitting by Highly Reduced Cerium Oxide: The Role of O Vacancy Coordination. *ACS Catal.* **2018**, *8* (5), 4354–4363. <https://doi.org/10.1021/acscatal.7b04409>.
- (38) Matz, O.; Calatayud, M. Breaking H₂ with CeO₂: Effect of Surface Termination. *ACS Omega* **2018**, *3* (11), 16063–16073. <https://doi.org/10.1021/acsomega.8b02410>.
- (39) Vecchiotti, J.; Baltanás, M. A.; Gervais, C.; Collins, S. E.; Blanco, G.; Matz, O.; Calatayud, M.; Bonivardi, A. Insights on Hydride Formation over Cerium-Gallium Mixed Oxides: A Mechanistic Study

for Efficient H₂ Dissociation. *J. Catal.* **2017**, *345*, 258–269. <https://doi.org/10.1016/j.jcat.2016.11.029>.

(40) Pacchioni, G. Numerical Simulations of Defective Structures: The Nature of Oxygen Vacancy in Non-Reducible (MgO, SiO₂, ZrO₂) and Reducible (TiO₂, NiO, WO₃) Oxides. In *Defects at Oxide Surfaces*; Jupille, J., Thornton, G., Eds.; Springer International Publishing: Cham, 2015; Vol. 58, pp 1–28. https://doi.org/10.1007/978-3-319-14367-5_1.

(41) Barteau, M. A. Organic Reactions at Well-Defined Oxide Surfaces. *Chem. Rev.* **1996**, *96* (4), 1413–1430. <https://doi.org/10.1021/cr950222t>.

(42) Calatayud, M.; Markovits, A.; Menetrey, M.; Mguig, B.; Minot, C. Adsorption on Perfect and Reduced Surfaces of Metal Oxides. *Catal. Today* **2003**, *85* (2–4), 125–143. [https://doi.org/10.1016/S0920-5861\(03\)00381-X](https://doi.org/10.1016/S0920-5861(03)00381-X).

(43) Kresse, G.; Hafner, J. *Ab Initio* Molecular Dynamics for Liquid Metals. *Phys. Rev. B* **1993**, *47* (1), 558–561. <https://doi.org/10.1103/PhysRevB.47.558>.

(44) Kresse, G.; Hafner, J. *Ab Initio* Molecular-Dynamics Simulation of the Liquid-Metal–Amorphous-Semiconductor Transition in Germanium. *Phys. Rev. B* **1994**, *49* (20), 14251–14269. <https://doi.org/10.1103/PhysRevB.49.14251>.

(45) Kresse, G.; Furthmüller, J. Efficiency of Ab-Initio Total Energy Calculations for Metals and Semiconductors Using a Plane-Wave Basis Set. *Comput. Mater. Sci.* **1996**, *6* (1), 15–50. [https://doi.org/10.1016/0927-0256\(96\)00008-0](https://doi.org/10.1016/0927-0256(96)00008-0).

(46) Kresse, G.; Furthmüller, J. Efficient Iterative Schemes for *Ab Initio* Total-Energy Calculations Using a Plane-Wave Basis Set. *Phys. Rev. B* **1996**, *54* (16), 11169–11186. <https://doi.org/10.1103/PhysRevB.54.11169>.

(47) Blöchl, P. E. Projector Augmented-Wave Method. *Phys. Rev. B* **1994**, *50* (24), 17953–17979. <https://doi.org/10.1103/PhysRevB.50.17953>.

(48) Kresse, G.; Joubert, D. From ultrasoft pseudopotentials to the projector augmented-wave method. *Phys. Rev. B* **1999**, *59* (3), 1758–1775. <https://doi.org/10.1103/PhysRevB.59.1758>.

(49) Kullgren, J.; Castleton, C. W. M.; Müller, C.; Ramo, D. M.; Hermansson, K. B3LYP Calculations of Cerium Oxides. *J. Chem. Phys.* **2010**, *132* (5), 054110. <https://doi.org/10.1063/1.3253795>.

(50) Skorodumova, N. V.; Ahuja, R.; Simak, S. I.; Abrikosov, I. A.; Johansson, B.; Lundqvist, B. I. Electronic, Bonding, and Optical Properties of CeO₂ and Ce₂O₃ from First Principles. *Phys. Rev. B* **2001**, *64* (11). <https://doi.org/10.1103/PhysRevB.64.115108>.

(51) Perdew, J. P.; Burke, K.; Ernzerhof, M. Generalized Gradient Approximation Made Simple. *Phys. Rev. Lett.* **1996**, *77* (18), 3865–3868. <https://doi.org/10.1103/PhysRevLett.77.3865>.

(52) Perdew, J. P.; Burke, K.; Ernzerhof, M. Generalized Gradient Approximation Made Simple [Phys. Rev. Lett. *77*, 3865 (1996)]. *Phys. Rev. Lett.* **1997**, *78* (7), 1396–1396. <https://doi.org/10.1103/PhysRevLett.78.1396>.

- (53) Henkelman, G.; Uberuaga, B. P.; Jónsson, H. A Climbing Image Nudged Elastic Band Method for Finding Saddle Points and Minimum Energy Paths. *J. Chem. Phys.* **2000**, *113* (22), 9901–9904. <https://doi.org/10.1063/1.1329672>.
- (54) Henkelman, G.; Jónsson, H. Improved Tangent Estimate in the Nudged Elastic Band Method for Finding Minimum Energy Paths and Saddle Points. *J. Chem. Phys.* **2000**, *113* (22), 9978–9985. <https://doi.org/10.1063/1.1323224>.
- (55) Henkelman, G.; Jónsson, H. A Dimer Method for Finding Saddle Points on High Dimensional Potential Surfaces Using Only First Derivatives. *J. Chem. Phys.* **1999**, *111* (15), 7010–7022. <https://doi.org/10.1063/1.480097>.
- (56) Heyden, A.; Bell, A. T.; Keil, F. J. Efficient Methods for Finding Transition States in Chemical Reactions: Comparison of Improved Dimer Method and Partitioned Rational Function Optimization Method. *J. Chem. Phys.* **2005**, *123* (22), 224101. <https://doi.org/10.1063/1.2104507>.
- (57) Baroni, S.; de Gironcoli, S.; Dal Corso, A.; Giannozzi, P. Phonons and Related Crystal Properties from Density-Functional Perturbation Theory. *Rev. Mod. Phys.* **2001**, *73* (2), 515–562. <https://doi.org/10.1103/RevModPhys.73.515>.
- (58) Karhánek, D.; Bučko, T.; Hafner, J. A Density-Functional Study of the Adsorption of Methane-Thiol on the (111) Surfaces of the Ni-Group Metals: II. Vibrational Spectroscopy. *J. Phys. Condens. Matter* **2010**, *22* (26), 265006. <https://doi.org/10.1088/0953-8984/22/26/265006>.
- (59) Huntelaar, M. E.; Booij, A. S.; Cordfunke, E. H. P.; van der Laan, R. R.; van Genderen, A. C. G.; van Miltenburg, J. C. The Thermodynamic Properties of $\text{Ce}_2\text{O}_3(\text{s})$ from $T \rightarrow 0$ K to 1500 K. *J. Chem. Thermodyn.* **2000**, *32* (4), 465–482. <https://doi.org/10.1006/jcht.1999.0614>.
- (60) Mullins, D. R. The Surface Chemistry of Cerium Oxide. *Surf. Sci. Rep.* **2015**, *70* (1), 42–85. <https://doi.org/10.1016/j.surfrep.2014.12.001>.
- (61) Monkhorst, H. J.; Pack, J. D. Special Points for Brillouin-Zone Integrations. *Phys. Rev. B* **1976**, *13* (12), 5188–5192. <https://doi.org/10.1103/PhysRevB.13.5188>.
- (62) Pinto, H.; Mintz, M. H.; Melamud, M.; Shaked, H. Neutron Diffraction Study of Ce_2O_3 . *Phys. Lett. A* **1982**, *88* (2), 81–83. [https://doi.org/10.1016/0375-9601\(82\)90596-5](https://doi.org/10.1016/0375-9601(82)90596-5).
- (63) Bärnighausen, H.; Schiller, G. The Crystal Structure of A- Ce_2O_3 . *J. Common Met.* **1985**, *110* (1–2), 385–390. [https://doi.org/10.1016/0022-5088\(85\)90347-9](https://doi.org/10.1016/0022-5088(85)90347-9).
- (64) Fabris, S.; de Gironcoli, S.; Baroni, S.; Vicario, G.; Balducci, G. Taming Multiple Valency with Density Functionals: A Case Study of Defective Ceria. *Phys. Rev. B* **2005**, *71* (4). <https://doi.org/10.1103/PhysRevB.71.041102>.
- (65) Mikami, M.; Nakamura, S. Electronic Structure of Rare-Earth Sesquioxides and Oxysulfides. *J. Alloys Compd.* **2006**, *408–412*, 687–692. <https://doi.org/10.1016/j.jallcom.2005.01.068>.
- (66) Hay, P. J.; Martin, R. L.; Uddin, J.; Scuseria, G. E. Theoretical Study of CeO_2 and Ce_2O_3 Using a Screened Hybrid Density Functional. *J. Chem. Phys.* **2006**, *125* (3), 034712. <https://doi.org/10.1063/1.2206184>.

- (67) Loschen, C.; Carrasco, J.; Neyman, K. M.; Illas, F. First-Principles LDA + U and GGA + U Study of Cerium Oxides: Dependence on the Effective U Parameter. *Phys. Rev. B* **2007**, *75* (3). <https://doi.org/10.1103/PhysRevB.75.035115>.
- (68) Andersson, D. A.; Simak, S. I.; Johansson, B.; Abrikosov, I. A.; Skorodumova, N. V. Modeling of CeO₂, Ce₂O₃, and CeO_{2-x} in the LDA+U Formalism. *Phys. Rev. B* **2007**, *75* (3), 035109. <https://doi.org/10.1103/PhysRevB.75.035109>.
- (69) Da Silva, J. L. F.; Ganduglia-Pirovano, M. V.; Sauer, J.; Bayer, V.; Kresse, G. Hybrid Functionals Applied to Rare-Earth Oxides: The Example of Ceria. *Phys. Rev. B* **2007**, *75* (4). <https://doi.org/10.1103/PhysRevB.75.045121>.
- (70) Graciani, J.; Márquez, A. M.; Plata, J. J.; Ortega, Y.; Hernández, N. C.; Meyer, A.; Zicovich-Wilson, C. M.; Sanz, J. F. Comparative Study on the Performance of Hybrid DFT Functionals in Highly Correlated Oxides: The Case of CeO₂ and Ce₂O₃. *J. Chem. Theory Comput.* **2011**, *7* (1), 56–65. <https://doi.org/10.1021/ct100430q>.
- (71) Helali, Z.; Jedidi, A.; Syzgantseva, O. A.; Calatayud, M.; Minot, C. Scaling Reducibility of Metal Oxides. *Theor. Chem. Acc.* **2017**, *136* (9). <https://doi.org/10.1007/s00214-017-2130-y>.
- (72) Nolan, M.; Fearon, J.; Watson, G. Oxygen Vacancy Formation and Migration in Ceria. *Solid State Ion.* **2006**, *177* (35–36), 3069–3074. <https://doi.org/10.1016/j.ssi.2006.07.045>.
- (73) Kullgren, J.; Hermansson, K.; Castleton, C. Many Competing Ceria (110) Oxygen Vacancy Structures: From Small to Large Supercells. *J. Chem. Phys.* **2012**, *137* (4), 044705. <https://doi.org/10.1063/1.4723867>.
- (74) Ganduglia-Pirovano, M. V.; Da Silva, J. L. F.; Sauer, J. Density-Functional Calculations of the Structure of Near-Surface Oxygen Vacancies and Electron Localization on CeO₂ (111). *Phys. Rev. Lett.* **2009**, *102* (2). <https://doi.org/10.1103/PhysRevLett.102.026101>.
- (75) Henkelman, G.; Arnaldsson, A.; Jónsson, H. A Fast and Robust Algorithm for Bader Decomposition of Charge Density. *Comput. Mater. Sci.* **2006**, *36* (3), 354–360. <https://doi.org/10.1016/j.commatsci.2005.04.010>.
- (76) Sanville, E.; Kenny, S. D.; Smith, R.; Henkelman, G. Improved Grid-Based Algorithm for Bader Charge Allocation. *J. Comput. Chem.* **2007**, *28* (5), 899–908. <https://doi.org/10.1002/jcc.20575>.
- (77) Tang, W.; Sanville, E.; Henkelman, G. A Grid-Based Bader Analysis Algorithm without Lattice Bias. *J. Phys. Condens. Matter* **2009**, *21* (8), 084204. <https://doi.org/10.1088/0953-8984/21/8/084204>.
- (78) Yu, M.; Trinkle, D. R. Accurate and Efficient Algorithm for Bader Charge Integration. *J. Chem. Phys.* **2011**, *134* (6), 064111.
- (79) Anderson, A. B.; Nichols, J. A. Hydrogen on Zinc Oxide. Theory of Its Heterolytic Adsorption. *J. Am. Chem. Soc.* **1986**, *108* (16), 4742–4746. <https://doi.org/10.1021/ja00276a010>.
- (80) Anchell, J. L.; Morokuma, K.; Hess, A. C. An Electronic Structure Study of H₂ and CH₄ Interactions with MgO and Li-doped MgO Clusters. *J. Chem. Phys.* **1993**, *99* (8), 6004–6013. <https://doi.org/10.1063/1.465899>.

- (81) Pisani, C.; D'ercole, A. Electrostatic Effects in the Heterolytic Dissociation of Hydrogen at Magnesium Oxide. In *New Trends in Quantum Systems in Chemistry and Physics*; Maruani, J., Minot, C., McWeeny, R., Smeyers, Y. G., Wilson, S., Eds.; Lipscomb, W. N., Prigogine, I., Maruani, J., Wilson, S., Ågren, H., Avnir, D., Cioslowski, J., Daudel, R., Gross, E. K. U., van Gunsteren, W. F., et al., Series Eds.; Springer Netherlands: Dordrecht, 2000; Vol. 7, pp 247–255. https://doi.org/10.1007/0-306-46950-2_14.
- (82) Syzgantseva, O. A.; Calatayud, M.; Minot, C. Revealing the Surface Reactivity of Zirconia by Periodic DFT Calculations. *J. Phys. Chem. C* **2012**, *116* (11), 6636–6644. <https://doi.org/10.1021/jp209898q>.
- (83) Santos, E.; Quaino, P.; Schmickler, W. Theory of Electrocatalysis: Hydrogen Evolution and More. *Phys. Chem. Chem. Phys.* **2012**, *14* (32), 11224. <https://doi.org/10.1039/c2cp40717e>.